Research on Time Series InSAR Monitoring Method for Multiple Types of Surface Deformation in Mining Area

Yaxing Li (yaxing_98@163.com)
China University of Mining and Technology Beijing Campus https://orcid.org/0000-0002-2730-1060
Keming Yang
China University of Mining and Technology Beijing Campus
Zhixian Hou
China University of Mining and Technology Beijing Campus
Shuang Wang
China University of Mining and Technology Beijing Campus
Xinming Ding
China University of Mining and Technology Beijing Campus
Jianhong Zhang
China University of Mining and Technology Beijing Campus

Research Article

Keywords: SBAS-InSAR, PS-InSAR, mining area, surface deformation, monitoring method

Posted Date: November 8th, 2021

DOI: https://doi.org/10.21203/rs.3.rs-992936/v1

Research on time series InSAR monitoring method for multiple types of surface deformation in mining area

LI Ya-xing, YANG Ke-ming*, HOU Zhi-xian, WANG Shuang, DING Xin-ming, ZHANG Jian-hong

College of Geoscience and Surveying Engineering，China University of Mining and Technology-Beijing，Beijing 100083，China

Abstract

Interferometric Synthetic Aperture Radar (InSAR) has become the main choice of remote sensing detection method for monitoring large surface subsidence and deformation caused by underground coal mining. Time Series InSAR (TS-InSAR) has been intensively researched in mining-caused deformation monitoring for its ability to provide surface deformation time series, with Short Baseline Subset InSAR (SBAS-InSAR) and Permanent Scatter InSAR (PS-InSAR) being two classical methods. To obtain the incline and curvature in mining areas and assess the building damage, this paper exploits the results from SBAS-InSAR and PS-InSAR methods for the estimation of surface incline and curvature, following the principle of directional derivatives, and the surface beneath the villages and the industrial square near the 7221 Grout-filled working face, in the Huaibei mining area of Anhui Province, China, was analyzed. The estimated surface incline and curvature with SBAS-InSAR were within the threshold values specified for Class I damage, while PS-InSAR showed less than 1% measurements which exceeded this threshold. This paper provides a method for monitoring the surface deformation beneath the buildings around the mine area. Meanwhile, the dynamic analysis of the damage degree of buildings provides a basis for the determination of the influence range with grout-filled working faces.

Keywords: SBAS-InSAR, PS-InSAR, mining area, surface deformation, monitoring method

1 Introduction

China is a large producer and consumer of mineral resources, but its large-scale development and exploitation has made a significant contribution to national economic and social development, while also seriously damaging the geological environment of mines, and directly affecting the effective use of land resources in mining areas and the safety of normal life of residents(Bell, Stacey, and Genske 2000). For the disaster monitoring method of surface deformation caused by mining, ordinary geodetic measurement (Sedlak and Sgem 2015; Wesolowski 2016; Gao et al. 2014; Li et al. 2018)and other means need to spend a lot of manpower and material resources, the observation results can only get discontinuous points as the basis of calculation data, it is difficult to achieve continuous monitoring on the plane area. The Interferometric Synthetic Aperture Radar (InSAR) technology proposed in the 1970s is a newly developed active microwave remote sensing earth observation technology in recent years (Bhattacharya and Mukherjee 2017; Moreira et al. 2013; Mastro et al. 2020), which can continuously monitor the mine area surface displacement with the help of image data obtained during the transit of SAR satellites. After recent decades of development, today's InSAR mainly include Digital Elevation Model (DEM) production(Zhang, Wang, and Chen 2012), differential InSAR (D-InSAR) (Wang et al. 2009) and time-series InSAR (TS-InSAR) deformation monitoring (Fan, Lu, and Yao 2018).InSAR deformation monitoring has been widely used to monitor surface deformation, such as mining(Yang et al. 2020; Sui, Ma, and Chen 2020), landslides(Castaneda et al. 2009), volcanic eruptions(Olivier et al. 2019; Comerci et al.

2015), glacial movements(Zhou et al. 2011; Li et al. 2009), spatial changes in sea level (Tang et al. 2021), and urban ground subsidence(Chen et al. 2021; Ding et al. 2021; Li et al. 2016).

Short Baseline Subset InSAR (SBAS-InSAR) and Permanent Scatter InSAR (PS-InSAR) have been widely used as two classical TS-InSARs. As far as mine surface deformation monitoring is concerned, SBAS-InSAR can make up for the problem of manpower consumption of GPS monitoring means in deformation monitoring of an open-pit mine in high cold and high altitude Tianshan, and the large monitoring range and high accuracy of sinking data obtained by SBAS-InSAR provide the theoretical basis for environmental restoration and safe construction (Du et al. 2021). The new time-series InSAR combined with the ascending and descending orbit data to analyze the surface deformation after mining located at the French and German borders, and the high-precision subsidence and uplift data identified more deformation areas and compensated for the insufficient number of level survey datum points(Samsonov, d'Oreye, and Smets 2013). The surface deformation values calculated by SBAS-InSAR were validated using GPS data at a mine site in Seoul, and the support vector regression algorithm used the validated surface deformation values for prediction to obtain high accuracy surface deformation predictions (Shi et al. 2020). Surface subsidence diagram and monitoring of villages near mining areas in India using the modified PS-InSAR has good practical results for monitoring the slow settlement of villages with high accuracy(Kumar et al. 2020). However, the above results are basically applied to the calculation of subsidence monitoring of the mine surface, while the calculation and analysis of the surface incline, curvature, and other deformation values are lacking.

The paper mentions that the damage level of buildings and evaluation indexes in the Cross Reference Table of Surface Structural Damage Levels and Ground Deformation is based on the actual calculated incline value, curvature value, and horizontal movement value of the ground in relation to the threshold value as a basis for judging the degree of damage to buildings (Diao et al. 2018). The result obtained by InSAR is the projection of line-of-sight deformation to vertical deformation, and the surface subsidence value of the mine area is obtained by this method, which cannot be directly applied to the evaluation of the level of structural damage of the surface buildings. The evaluation of building damage around the Fengfeng mine area was mainly calculated using the results of Sentinel-1A images, and the conversion formula between surface subsidence values and building deformation values was established to calculate the evaluation of building damage (Diao et al. 2018). The evaluation of building damage around the Panji coal mine was approximated by using the results of satellite image calculations combined with the field deployment of conductors and using the surface subsidence velocity and slope as evaluation factors to classify the surface building damage level (Li, Gao, and Lu 2019). PS-InSAR is applied in mining areas mainly with the help of artificial angular reflectors to calculate the PS (permanent scatterer) points time-series sedimentation values, and by establishing a closed loop of wire observations and applying geodesic theory for error analysis, it shows a good prospect of PS point application (Xing et al. 2013). The application of PS-InSAR is very limited due to the large value of surface deformation gradient in the mine area and the serious temporal-spatial decoherence of the mine features (Maghsoudi et al. 2018). Therefore, it is essential to use remote sensing technology to reasonably extract the "surface area" deformation data of buildings in mining areas, and apply the evaluation system based on surface deformation variables and building damage levels to evaluate and analyze the damage of buildings in the process of working face mining.

In this paper, with the help of Sentinel-1A, a total of 21 images data from October 11, 2017, to

June 22, 2018, SBAS-InSAR (Berardino et al. 2002; Fan, Lu, and Yao 2018) was used to select the pixels with coherence greater than 0.18 near the 7221 Grout-filled working face of a mine in Huaibei Mining Group, Anhui Province. The line-of-sight deformation was projected onto the vertical deformation to obtain the time series deformation diagram of the 7221 working face in this time period. Meanwhile, using PS-InSAR (Hooper et al. 2004; Hooper, Segall, and Zebker 2007; Ferretti, Prati, and Rocca 2000), PS points within the area of Gaochangying village, Houlou Gaojia village, and Industrial Square maintenance belt near the 7221 Grout-filled working face of the mine were selected to obtain the temporal settlement values of each PS point during the mining time period of the working face. Using the principles of directional derivatives and geodesy, each pixel or PS point is assumed to be a ground deformation observation conductor point, and the calculated diagrams of incline and curvature values corresponding to each period of the time series subsidence diagram are obtained. Referring to the Cross Reference Table of Surface Structural Damage Levels and Ground Deformation(Diao et al. 2018), it is possible to evaluate the building damage levels of buildings in villages and Industrial Square in the study area, and also to analyze the active period of surface deformation and the influence range of the surface deformation that occurs during the workings 7221 mined with overburden isolation grout filling technology according to the spatial distribution of the time when serious damage occurs to the buildings.

2 Methodology

2.1 SBAS-InSAR Methods

To limit temporal and spatial decoherence, the SBAS-InSAR combines small baseline interference pairs by setting a certain spatio-temporal baseline threshold, and inverse performs the optimal deformation phase sequence according to the minimum parametric criterion. Suppose that N+1 SAR images acquired in the same region in the time series (t_0, t_1, ..., t_n) have been acquired, and after setting a certain spatio-temporal baseline threshold, M Interference pairs can be formed, and M satisfies:

$$\frac{N+1}{2} \le M \le \frac{N(N+1)}{2} \tag{1}$$

SBAS-InSAR requires aligning all images to the same super master image and generating M differential interferograms images with multi-view processing, topographic differencing, and phase unwrapping before performing parametrics inversion. Now consider two SAR images acquired at moments t_A and t_B (assuming $t_A < t_B$) with differential j-interferogram. Without considering errors such as atmospheric delay, the interferometric phase composition of the pixels with coordinates *(x, r)* in the azimuthal and distance directions is:

$$\delta\varphi_j(x,r) = \varphi(t_B,x,r) - \varphi(t_A,x,r) \approx \frac{4\pi}{\lambda}[d(t_B,x,r) - d(t_A,x,r)] \tag{2}$$

where $\varphi(t_B,x,r)$ and $\varphi(t_A,x,r)$ are the phases of the corresponding SAR images at time t_B and t_A, $d(t_B,x,r)$ and $d(t_A,x,r)$ are the line-of-sight deformations at moments t_B and t_A with respect to moment t_0. To obtain a smooth and continuous solution, it is necessary to convert the phase in Eq. (2) to the form of the average phase velocity multiplied by the time baseline, i.e.

$$v_j(x,r)g(t_B - t_A) = \varphi(t_B,x,r) - \varphi(t_A,x,r) \tag{3}$$

where $v_j(x,r)$ denotes the average phase velocity of the *j*-interferogram. Thus, the phase of the *j*-interferogram can be expressed as the integral of the phase velocity across the time periods:

$$\delta\varphi_j(x,r) = \sum_{k=t_A}^{t_B-1} v_{k,k+1}(t_{k+1} - t_k) \tag{4}$$

So far, we can establish the observation equation connecting the phase velocity and *M* differential interference phases for each time period of (t_0, t_1, ...,t_n):

$$\mathbf{Bv} = \boldsymbol{\delta\varphi} \tag{5}$$

where $\boldsymbol{B}$ is the $M \times N$ coefficient matrix containing information on how the interferometric pairs are composed, $\boldsymbol{v}$ is the $N \times 1$ vector containing the phase velocity of each time period, and $\boldsymbol{\delta\varphi}$ is the $M \times 1$ vector containing the differential interferometric phase. If $\boldsymbol{B}$ is rank-deficient, Singular Value Decomposition (SVD) can be used to obtain the generalized inverse matrix of $\boldsymbol{B}$, and then obtain the minimum parametric solution of the deformation velocity.

2.2 PS-InSAR Methods

The basic idea of PS-InSAR is to screen out points that are only slightly affected by spatial and temporal decoherence in long time series, and the scattering characteristics of these points should remain stable. To implement this idea, Ferretti et al. first screened a series of PS candidate points by amplitude departure index D_A(Hooper et al. 2004; Hooper, Segall, and Zebker 2007; Ferretti, Prati, and Rocca 2000). This index is constructed considering that when the phase stability is high, the dispersion of the amplitude can better reflect the dispersion of the phase. After aligning the *N*+1 view SAR images covering the same area to the same master image, the D_A of a pixel is calculated as follows:

$$D_{\mathrm{A}} = \frac{\sigma_{\mathrm{A}}}{m_{\mathrm{A}}} \tag{6}$$

where σ_A and m_A denote the standard deviation and average value of the time series amplitude of the image *A* pixel. The smaller the D_A value represents the better the amplitude stability of the pixel, with better phase stability, usually the pixel with $D_A < 0.25$ is selected as the PS candidate point.

After the PS candidate points are identified, the Delaunay triangle network is constructed using these points. Assuming that the topographic phase has been roughly removed by the existing DEM, the relative differential *i*-interferogram between the PS point pairs (also called "arc segments") formed by the adjacent PS points *x* and *y* in the differential interferogram of view $\Delta\varphi^i_{x,y,\mathrm{int}}$ can be expressed as:

$$\begin{aligned}\Delta\varphi^i_{x,y,\mathrm{int}} &= \Delta\varphi^i_{x,y,\text{lin-disp}} + \Delta\varphi^i_{x,y,\Delta h} + \Delta\varphi^i_{x,y,\mathrm{res}} \\ &= \frac{4\pi}{\lambda}\left(t_i \cdot \Delta v_{x,y} + \frac{B^i_{\perp}}{R_i \sin\theta} \cdot \Delta h_{x,y}\right) + \Delta\varphi^i_{x,y,\mathrm{res}}\end{aligned} \tag{7}$$

where $\Delta\varphi^i_{x,y,\text{lin-disp}}$, $\Delta\varphi^i_{x,y,\Delta h}$ and $\Delta\varphi^i_{x,y,\mathrm{res}}$ denote the relative linear deformation phase, residual elevation phase, and other residual phases between the two points. The relative atmospheric delay, orbital error, nonlinear deformation, and other noise are mainly included in $\Delta\varphi^i_{x,y,\mathrm{res}}$. $B^i_{\perp}$, t_i

denote the spatial vertical baseline and the temporal baseline of the differential *i*-interferogram. λ, R_i, θ denote the wavelength, sensor-to-target distance, and radar incidence angle. $\Delta v_{x,y}$ denotes the relative deformation velocity between two points. $\Delta h_{x,y}$ denotes the relative residual elevation between the two points.

Orbital errors and atmospheric phases are strongly correlated in space, and residual terrain phases are also spatially correlated, so modeling for PS point pairs can effectively weaken their effects. In order to solve for $\Delta v_{x,y}$ and $\Delta h_{x,y}$ in Eq. (7), the time domain coherence $|\gamma_{x,y}|$ needs to be maximized:

$$\arg\max_{\Delta v_{x,y},\ \Delta h_{x,y}}\{|\gamma_{x,y}| = \frac{1}{N}\sum_{i=1}^{N} e^{\Delta\varphi^{i}_{x,y,\mathrm{int}} - \frac{4\pi}{\lambda}(t_i\cdot\Delta v_{x,y} + \frac{B^{i}_{\perp}}{R_i\sin\theta}\cdot\Delta h_{x,y})}\} \tag{8}$$

where *N* denotes the total number of PS point pairs. The periodogram method is generally used to solve Eq. (8) by first giving approximate upper and lower bounds for $\Delta v_{x,y}$ and $\Delta h_{x,y}$ then iterative sampling. Since the approximate upper and lower bounds of $\Delta v_{x,y}$ and $\Delta h_{x,y}$ are required, it is essential to have some knowledge of the study area. After estimating $\Delta v_{x,y}$ and $\Delta h_{x,y}$ for each arc segment, a certain path integral can be used to obtain the absolute deformation.

Using the low and high-frequency characteristics of atmospheric phase and orbital error in space and time, respectively, the atmospheric phase, orbital error, and nonlinear deformation in the residual phase can be separated by spatial and temporal filtering, and then the atmospheric phase and orbital error on each pixel of each interferogram can be estimated by spatial interpolation. After estimating and removing the atmospheric phase and orbit errors, the underestimation in analyzing the phase time domain stability has been mitigated. At this point, the final PS point can be selected based on the time domain coherence and amplitude dispersion at the same time, and the inversion is performed again to finally complete the measurement of the deformation field.

2.3 Surface incline and curvature deformation calculation

The magnitude of deformation of surface incline and curvature can be calculated based on the vertical deformation values of pixels and PS points. In areas where surface deformation is dominated by subsidence, such as mining areas, the obtained line-of-sight deformation to subsidence can generally be converted to subsidence in a direction perpendicular to the surface by the following equation:

$$d_v = d_{los}/\cos\theta \tag{9}$$

where d_{los} denotes the line-of-sight deformation measured by SBAS-InSAR, θ is the local angle of incidence of the SAR satellite. d_v denotes deformation perpendicular to the ground surface, a negative value indicates ground subsidence, a positive value indicates ground uplift.

1. inversion for surface incline with SBAS-InSAR

In the conventional surface deformation calculation of the measured data, the incline between two measurement points is the ratio of the difference between the subsidence of two points and the horizontal distance between these two points before deformation, and the calculated inclination is the incline between two observation points, not the inclination on a certain observation point. By treating each pixel in the SBAS-InSAR deformation diagram as an approximate surface deformation observation line point, the vertical deformation value of the pixel is equivalent to the subsidence value measured by the ground observation point in the corresponding time period, and the distance between the centers of adjacent pixels in the SBAS-InSAR deformation diagram is equivalent to the distance between adjacent observation points. Therefore, similar to the calculation method of surface deformation of conventional measured data, the surface incline value between two pixels can be obtained by dividing the differencing vertical deformation of adjacent pixels by the distance between the center points of adjacent pixels. The incline is the first-order derivative of the subsidence with respect to the horizontal distance from the surface. In this paper, the incline on a certain pixel should be calculated by an interval centered on that pixel. The incline value of any point *(m,n)* in the deformation diagram along the coordinate axis is calculated by the least-squares fitting method, assuming that the positive directions of the x and y axes of the plane's right-angle coordinate system are parallel to the east and north directions of the deformation diagram. The direction along the x positive semi-axis is as an example:

$$i_x(m,n) = -f_x(m,n)/R_x \tag{10}$$

where $i_x(m,n)$ denotes the incline value of the point *(m,n)* along the positive direction of the x-axis, $f_x(m,n)$ is the first-order partial derivative in the direction of the x-axis at the point *(m,n)* of the subsidence diagram. R_x is the distance between two adjacent pixels.

For the surface incline in any direction, the surface moving basin can be considered as a two-dimensional surface, then the incline of the surface along the coordinate axis direction is the same size and opposite direction of the first-order partial derivatives of the sinking in the x and y-axis directions. From the definition of the first-order directional derivative, it can be similarly deduced that:

$$i(\beta,m,n) = i_x(m,n)\cos\beta + i_y(m,n)\sin\beta \tag{11}$$

where $i(\beta,m,n)$ denotes the incline of the *(m,n)* point along the angle of β direction.

Maximum incline for a point on the surface and its direction:

$$\begin{cases} i'(m,n) = \left|(i_x(m,n), i_y(m,n))\right| \\ \beta'(m,n) = \arctan\dfrac{i_y(m,n)}{i_x(m,n)} \end{cases} \tag{12}$$

where $i'(m,n)$ denotes the absolute value of the maximum incline of the point *(m,n)*, which is called the maximum incline value, $\beta'(m,n)$ is the maximum inclined azimuth of the point *(m,n)*, "|*|" means modulo the vector " * ".

2. inversion for surface curvature with SBAS-InSAR

Curvature is generated by the uneven surface incline and reflects the degree of curvature of the surface convexity and concavity. In mining subsidence observation, the surface curvature is the

ratio of the difference in the incline of two adjacent line segments to the sum of the lengths of the two-line segments before deformation. The curvature is the second-order derivative of the subsidence with respect to the horizontal distance from the surface. The curvature of a point on the ground along any direction can be calculated according to the second-order directional derivative formula:

$$K(\beta,m,n) = -[f_{xx}(m,n)\cos^2\beta/R_x^2 + 2f_{xy}(m,n)\cos\beta\sin\beta/(R_xR_y) + f_{yy}(m,n)\sin^2\beta/R_y^2] \quad (13)$$

where $K(\beta, m, n)$ denotes the curvature of the angle along β direction at the point (m,n), with positive values for convexity on the surface and negative values for depression on the surface. $f_{xx}(m, n)$, $f_{yy}(m, n)$ and $f_{xy}(m, n)$ are the second-order partial derivatives of the sink at the point (m,n) along the x-axis, the second-order partial derivatives of the sink at the point (m,n) along the y-axis and the second-order mixed partial derivatives of the sink at the point (m,n) along the x- and y-axes. The second-order partial derivative is solved similarly to Eq. (10). For the maximum curvature and its direction at a point j on the surface, the solution is as follows:

$$\left.\begin{aligned} &K'(m,n) = K(\beta_j,m,n) \\ &\left|K(\beta_j,m,n)\right| = \max[\left|K(\beta_1,m,n)\right|,\left|K(\beta_2,m,n)\right|,\ldots] \qquad j=1,2,\ldots \end{aligned}\right\} \quad (14)$$

where β_1, β_2, ... are all values of β that allow Eq. (14) to hold, $K'(m, n)$ is the maximum curvature at point j, β_j is the orientation angle of the maximum curvature value at point j.

3. inversion for surface incline and curvature with PS-InSAR

The PS points in the mine area are used to obtain the maximum incline and curvature values of the ground surface, and the PS points are equated to the geodetic surface deformation observation conductor points. Using the principle of permutation, the surface incline between two PS points can be obtained by traversing any two PS points whose differential distances are satisfied, and the incline is the first-order derivative of the subsidence with respect to the horizontal distance from the surface. In this paper, it is considered that the incline value between a certain pair of two PS points, should be calculated by using the two PS points as an interval endpoint.

The calculated incline value in the interval and the endpoints of the interval (the two PS points of the interval) are considered as two observation conductor points and an observation interval in the deployed ground deformation observation conductor. Using the permutation principle, two observation intervals are selected, containing a total of four observation lead points (four PS points), and the two observation intervals are required to have an identical endpoint (there exists an overlap of two PS points), thus forming a curvature value calculation interval. In mining subsidence observation, the surface curvature is the ratio of the difference in incline value of two adjacent line segments to the sum of the lengths of the two-line segments before deformation.

2.4 Ground deformation for building damage level evaluation

Ground deformation can trigger cracks in the walls of buildings, seriously affecting the safety of building occupants. Based on the relevant references of national safety codes and building protection evaluation, the Cross Reference Table of Surface Structural Damage Levels and Ground Deformation(Diao et al. 2018) was cited to obtain the ground reference deformation for building damage level evaluation, as shown in Table 1.

The incline value within the interval calculated by the two PS point pairs (the inclination value

calculated by the two "surface deformation observation guide points") can be compared with the surface incline threshold value in Table 1 as the surface deformation index for evaluating the damage of buildings within the interval. The curvature value of the interval can be compared with the surface curvature threshold in Table 1 as an indicator to evaluate the degree of building damage within the interval, and a diagram can also be made to observe the spatial distribution of PS points in the interval exceeding the specified threshold to obtain a diagram of the spatial distribution of building vulnerability areas.

Table 1 Cross Reference Table of Surface Structural Damage Levels and Ground Deformation

Damage grade	Description of damaged constructions	Ground deformation value		
		Incline (mm/ m^{-1})	Curvature (*10^{-3} m^{-1})	Horizontal deformation (mm/ m^{-1})
I	Cracks in walls of masonry buildings <4mm in width and total width of multiple cracks <10 mm	≤ 3.0	≤ 0.2	≤ 2.0
II	Cracks in walls of masonry buildings <15mm in width and total width of multiple cracks <30 mm	≤6.0	≤ 0.4	≤ 4.0
III	Cracks in walls of masonry buildings <30mm in width and total width of multiple cracks <50 mm	≤10.0	≤ 0.6	≤ 6.0
IV	Cracks in walls of masonry buildings ≥30mm in width and total width of multiple cracks ≥50 mm	>10	>0.6	>6.0

3 Study area

The study area is located at the surface of the 82 mining area of a mine of Huaibei Mining Group in Anhui Province, which is located in the territory of Guoyang County, Bozhou City, Anhui Province, and the 82 mining area is located in the middle and south of the mine. The 7221 working face is located about 160m west of Houlou Gaojia Village and about 400m south of Gaochangying Village, as shown in Figure 1. The 7221 working face was mined using overburden isolation grout filling technology to reduce surface subsidence due to the mining of the working face, which started on December 6, 2017, and ended on June 3, 2018. The working face contains five grouting holes, the southern part of the working face distributes grouting holes No. 1 and No. 2 with grouting cycles from January 8, 2018, to March 12, 2018, and from January 29, 2018, to July 14, 2018,the northern part of the working face distributes grouting holes No. 3, No. 4, and No. 5 with grouting cycles from March 22, 2018, to May 22, 2018, March 16 to July 14, 2018, April 17, 2018, to July 14, 2018.

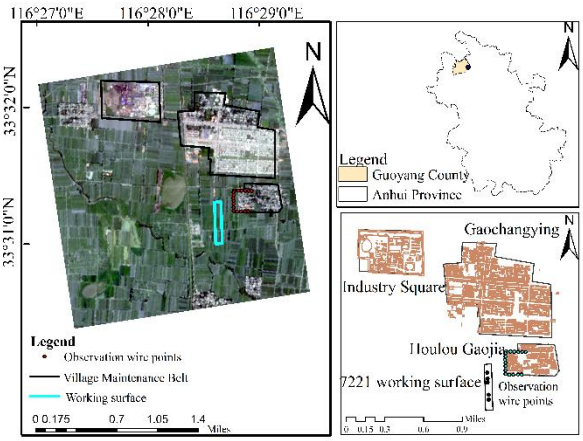

Figure 1 Schematic diagram of the geographical location of the study area

4 Results analysis of SBAS-InSAR

A total of 21 views of Sentinel-1A images were selected from October 11, 2017 to June 20, 2018, and the time threshold was set to 24 days to obtain the time-space baseline diagram shown in Figure 2.

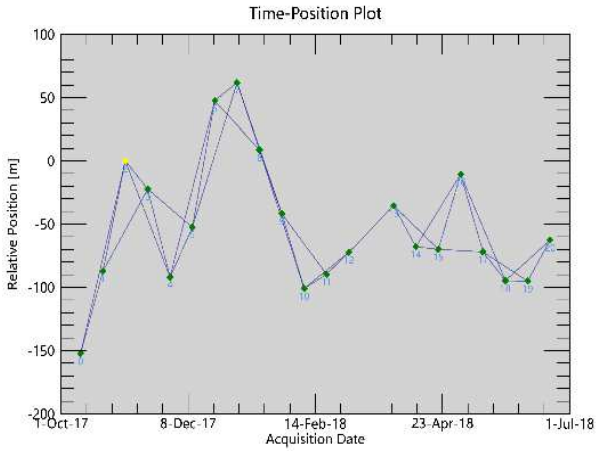

Figure 2 SBAS-InSAR time-space baseline diagram

The subsidence diagram calculated by SBAS-InSAR, as shown in Fig. 3(a)-(g), shows that one month after the mining of the 7221 grouted working face, subsidence began to appear on the surface south of the working face. At this time, due to the small effect of coal seam mining on surface subsidence, the subsidence area is only near the working face of 7221. And from Fig. 3(h)-(o), it can be seen that although the mining of 7211 working face has reached the active period, the speed of surface subsidence has accelerated and the range of surface subsidence basin is expanding. Since the grouting activity of the grouting holes at the working face, the surface subsidence of the nearby villages is well controlled, and the influence of coal seam mining on surface subsidence has still not reached the nearest Houlou Gaojia village at this time, the overall Houlou Gaojia village has no obvious subsidence. From the last five subsidence diagrams in Figure 3(p)-(t), it can be found that due to the coal seam mining at the 7221 working face and the grouting activity of the grouting hole, which makes the surface activity intense at this time, a large area of the surface subsidence phenomenon, the subsidence range has entered the interior of Houlou Gaojia village, the village is affected by the mining at the 7221 working face but for the analysis of the severity of damage to the village buildings, it cannot be directly obtained from the analysis in Figure 3 Conclusion.

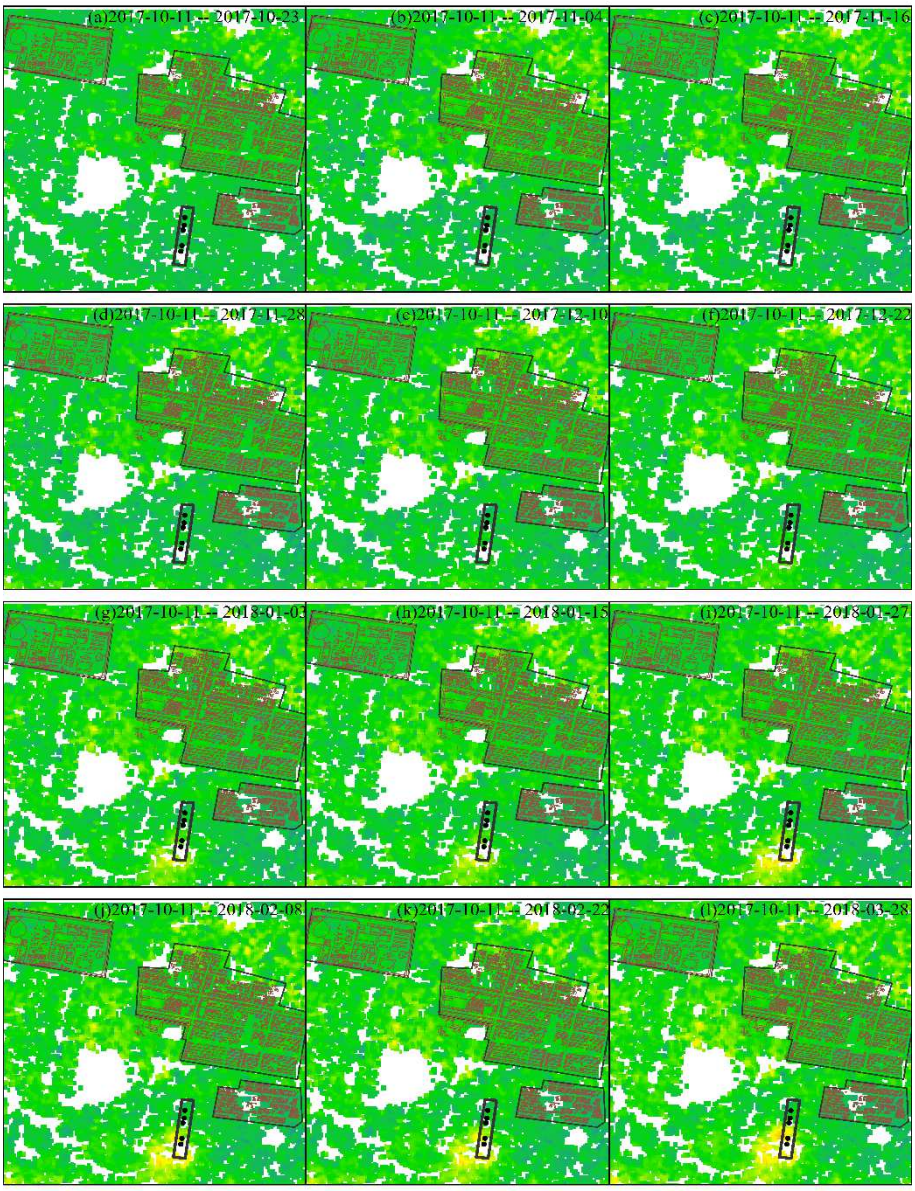
(a)2017-10-11 – 2017-10-23
(b)2017-10-11 – 2017-11-04
(c)2017-10-11 – 2017-11-16
(d)2017-10-11 – 2017-11-28
(e)2017-10-11 – 2017-12-10
(f)2017-10-11 – 2017-12-22
(g)2017-10-11 – 2018-01-03
(h)2017-10-11 – 2018-01-15
(i)2017-10-11 – 2018-01-27
(j)2017-10-11 – 2018-02-08
(k)2017-10-11 – 2018-02-22
(l)2017-10-11 – 2018-03-28

1

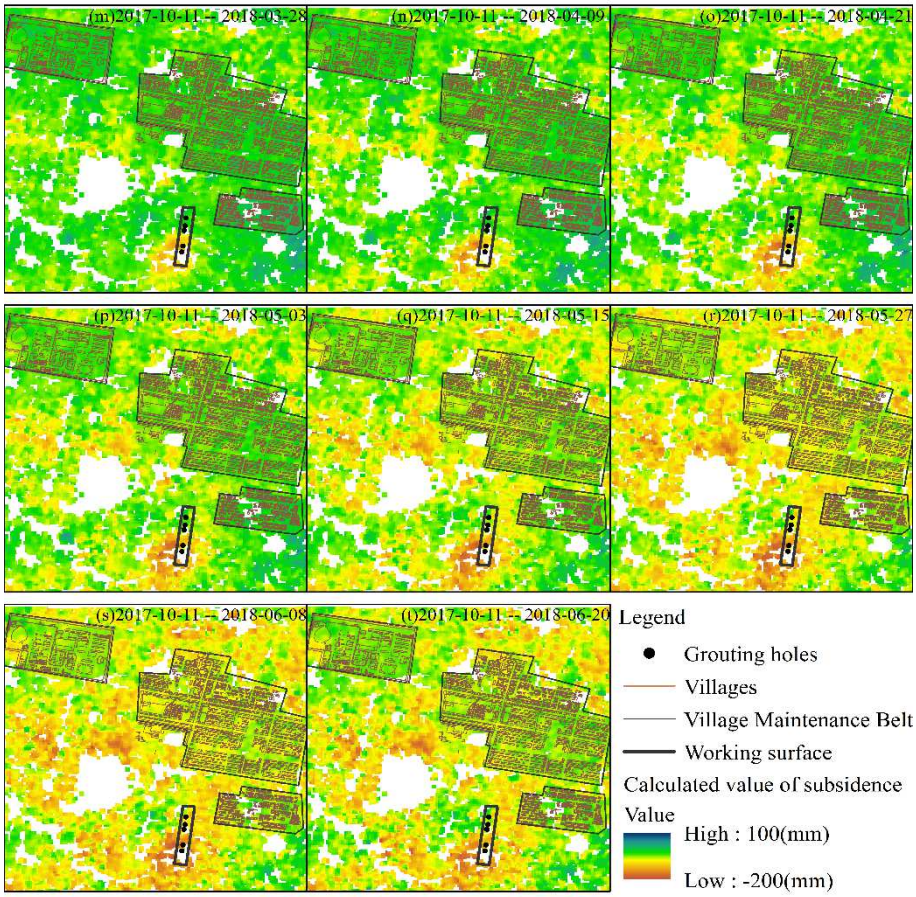

Figure 3 SBAS-InSAR time series subsidence diagram of working face 7221

With the help of directional derivative and geodesy, the subsidence diagram obtained by SBAS-InSAR was further calculated and analyzed to obtain the maximum incline value and maximum curvature value calculation diagram during the mining cycle of 7221 grouting working face, as shown in Figure 4 and Figure 5.

The area showing blank in Figure 4 is the area of lower coherence such as water bodies. Evaluate the threshold value of 3mm/m for surface incline division between Class I damage and Class II damage of buildings in the mine area. The buildings in the villages of Gaochangying, Houlou Gaojia, and the Industrial Square maintenance belt near the 7221 working face as a whole are within the prescribed threshold of Class I damage. To analyze in more detail the impact of overburden grout filling mining technology on the surface deformation and nearby buildings, this paper divides the color band of the surface incline value of buildings within the tilt value of Class I damage threshold into three additional segments. This paper does not calculate the results of incline values along the mining direction and incline direction of the working face but focuses on the calculation of the maximum incline value of the ground surface, which facilitates the comparison and analysis with the reference table of the damage level of the ground surface structure and ground deformation.

The images time period selected for this paper contains the mining cycle of work face 7221, which was mined on December 6, 2017, until June 3, 2018, when the work face stopped mining. From the analysis of Fig. 4(a)-(g), it is concluded that the working face 7221 was mined from south to north, and the grouting holes did not start grouting activities at this time. The southwestern part of Houlou Gaojia Village, which is the closest to the working face during this period, was also not

affected by mining, which is consistent with the observation of the subsidence diagram. From (h)-(m) in Fig. 4, it can be seen that the working face was mined for nearly two months, and the two grouting holes in the south of the working face started grouting for nearly one month. Some pixels with surface incline values exceeding 3mm/m appeared around the surface.7221 The surface around the south of the working face started to enter the active period, while for the maintenance belt of the village of Hulou Gaojia Village, which is closer to the working face, the incline value exceeding the threshold value specified for Class I damage still did not appear at this time. It can be concluded from Figure 4(n)-(q) that the 7221 working face continues to be mined to the north and the grouting holes in the north begin to be grouted, at which time the incline value becomes larger in the western part of Houlou Gaojia village. The northeastern village maintenance belt of Gaochangying and Houlou Gaojia gradually reaches the incline value of secondary damage due to the influence of unknown workings mining, and the buildings should be monitored and protected with emphasis. From the analysis of Fig. 4(r)-(t), it is concluded that the working face mining reached the last month, the three grouting holes in the north exceeded one month, and the surface movement changed dramatically. The southwestern part of Houlou Gaojia Village is in the active range of surface movement and is affected by surface movement and deformation, so the buildings located in the southwestern part of Houlou Gaojia Village should be monitored and protected.

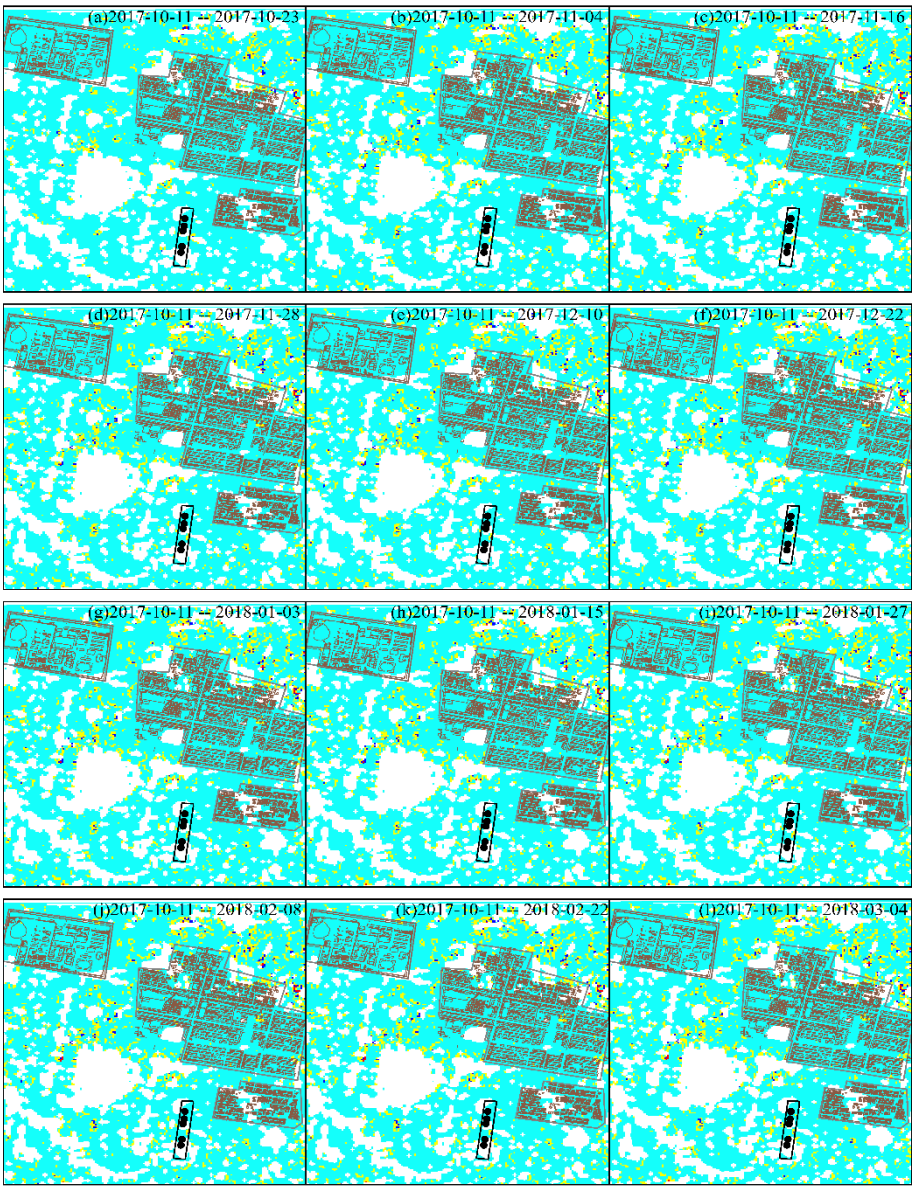
(a)2017-10-11 -- 2017-10-23
(b)2017-10-11 -- 2017-11-04
(c)2017-10-11 -- 2017-11-16
(d)2017-10-11 -- 2017-11-28
(e)2017-10-11 -- 2017-12-10
(f)2017-10-11 -- 2017-12-22
(g)2017-10-11 -- 2018-01-03
(h)2017-10-11 -- 2018-01-15
(i)2017-10-11 -- 2018-01-27
(j)2017-10-11 -- 2018-02-08
(k)2017-10-11 -- 2018-02-22
(l)2017-10-11 -- 2018-03-04

1

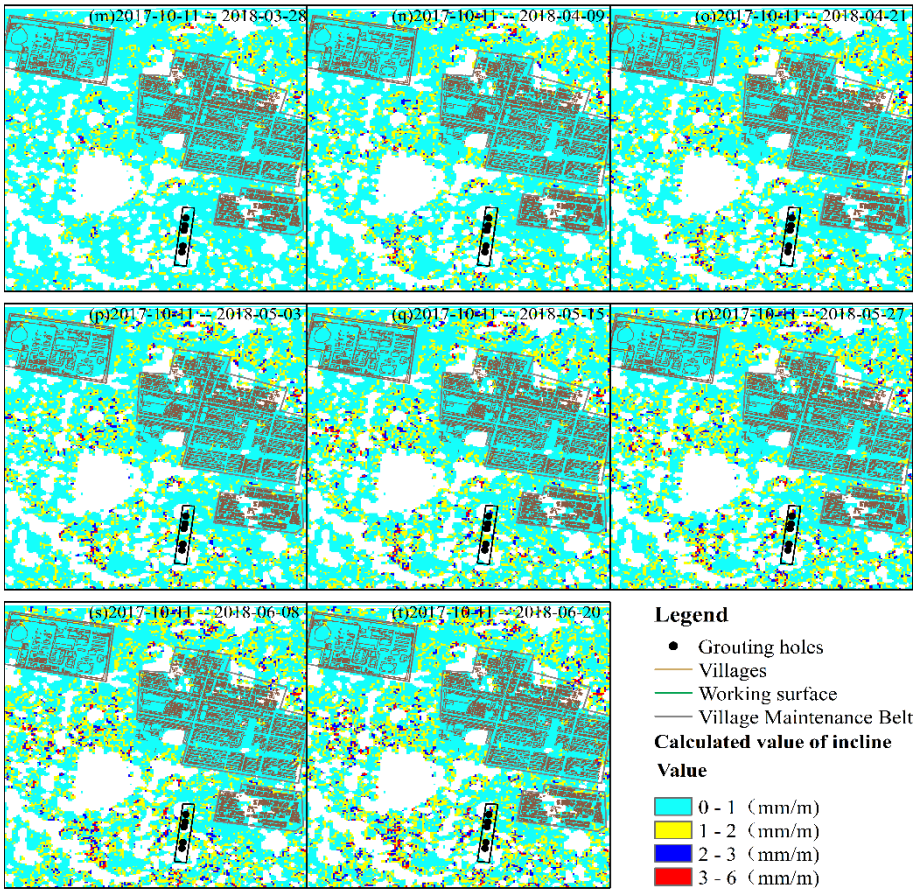

Fig. 4 SBAS-InSAR time series calculated incline values Diagram of working face 7221

The blanks in Figure 5 show low coherence and curvature values of -0.05 to 0.05 ($\times 10^{-3}$/m) pixels within the building protection line, which are not considered in general. Since the curvature takes positive or negative values to represent surface raise or depression, the images of curvature values calculated using SBAS-InSAR subsidence diagrams were divided into positive and negative pixel curvature values. The village of Gaochangying near the 7221 working face, the village of Houlou Gaojia and the buildings within the maintenance belt of the Industrial Square as a whole are all within the threshold of primary damage. To analyze in more detail the surface deformation and building damage of overlying isolated rock grout filling mining, this paper will add three segments to the color banding of building curvature values within the first level of damage.

From Figure 5(a)-(l), it can be seen that only a part of the area north of Gaochangying village appears to have a high curvature value, which is far away from the mining of 7221 working face and not caused by the mining of 7221 working face. From Figure 5(m)-(t), it can be seen that the surface movement is more active in the west and north of Houlou Gaojia Village, and the buildings in the maintenance belt of the village have not reached the first level of destruction, although the surface subsidence is caused by the mining of the 7221 working face. The surface is affected by the simultaneous subsidence and uplift due to the grouting action of the three grouting holes in the north of the 7221 working face. The buildings are easily damaged by surface deformation during this time period. For the key buildings in the southwestern part of the village, wires should be deployed to shorten the observation period and conduct high-precision and comprehensive observation, to strengthen the key protection of the buildings in this area.

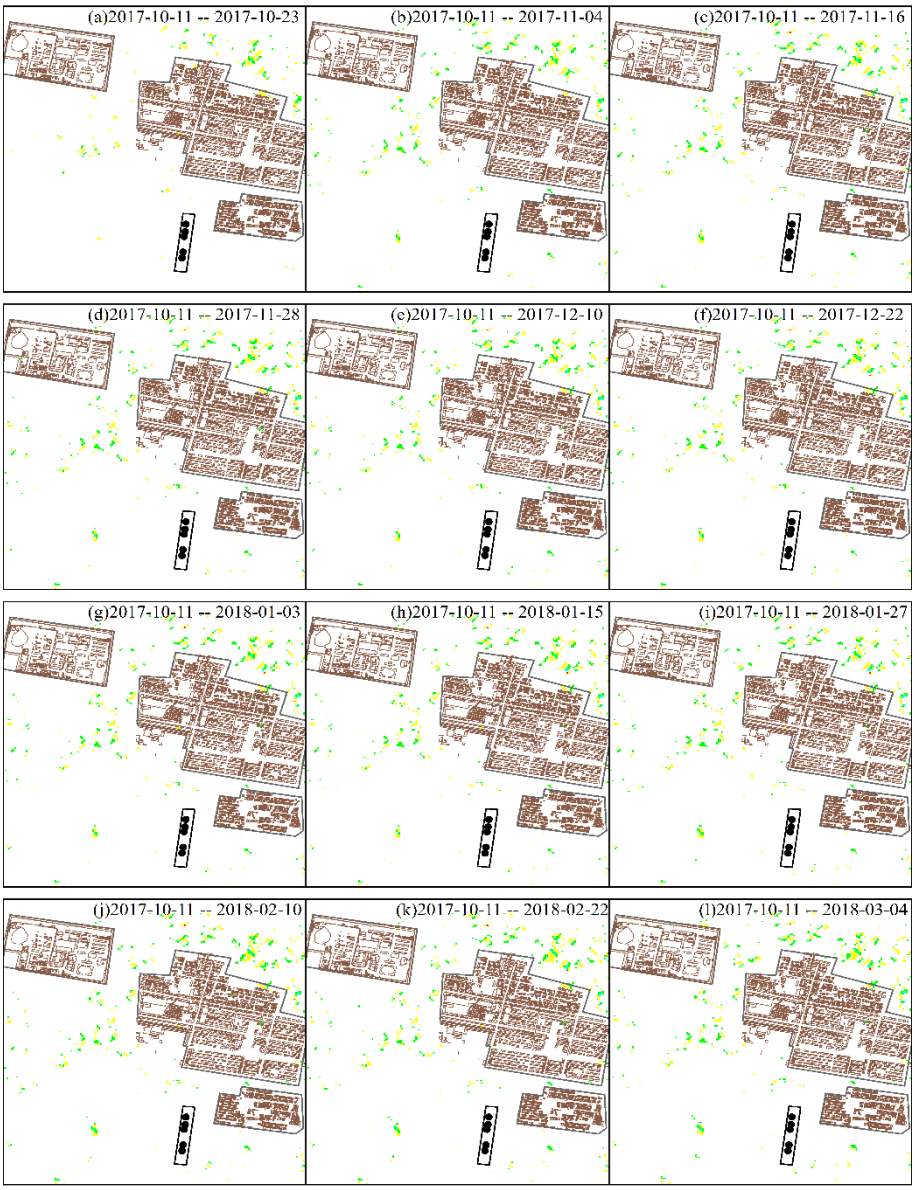
(a)2017-10-11 -- 2017-10-23
(b)2017-10-11 -- 2017-11-04
(c)2017-10-11 -- 2017-11-16
(d)2017-10-11 -- 2017-11-28
(e)2017-10-11 -- 2017-12-10
(f)2017-10-11 -- 2017-12-22
(g)2017-10-11 -- 2018-01-03
(h)2017-10-11 -- 2018-01-15
(i)2017-10-11 -- 2018-01-27
(j)2017-10-11 -- 2018-02-10
(k)2017-10-11 -- 2018-02-22
(l)2017-10-11 -- 2018-03-04

1

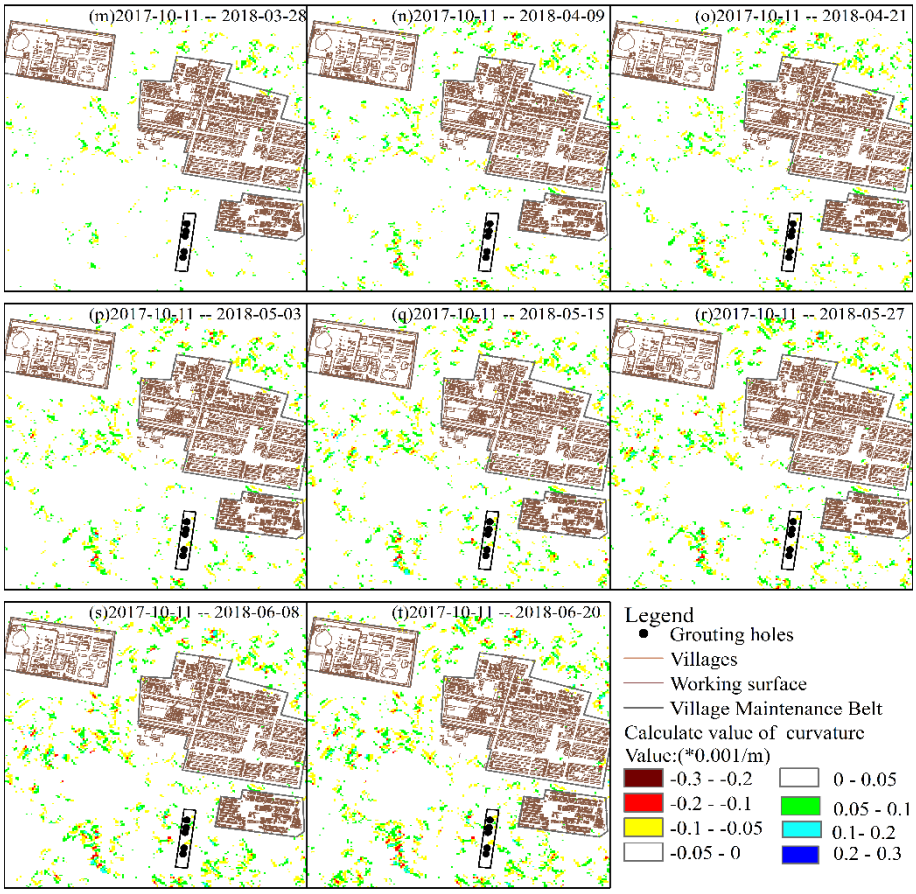

Figure 5 SBAS-InSAR time series calculated curvature values Diagram of working face 7221

5 Results analysis of PS-InSAR

Again, the data were selected from October 11, 2017, to June 20, 2018, with 21 views of Sentinel-1A images, set with the same SBAS-InSAR time threshold of 24 days, to obtain the time-space baseline diagram shown in Figure 6.

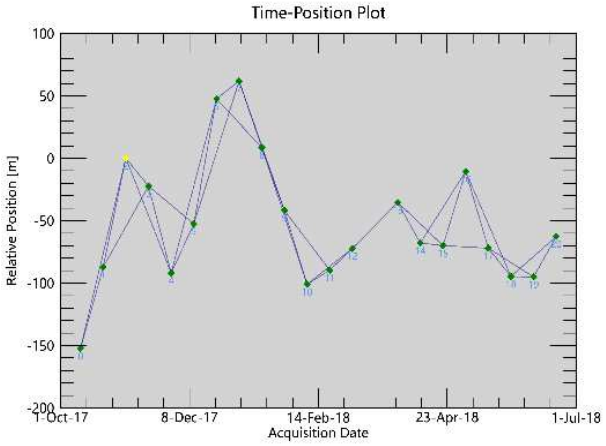

Figure 6 PS-InSAR time-space baseline diagram

As the calculated PS points are sparsely distributed near the working face, the value available for reference is low, and the focus is on selecting the PS points within the maintenance belt of Gaochangying village, Houlou Gaojia village, and the Industrial Square for analysis. The calculation shows that 257 PS points were obtained from Houlou Gaojia Village, 3,186 PS points

were obtained from Gaochangying Village, and 1,696 PS points were obtained from Industrial Square, as shown in Figure 7.

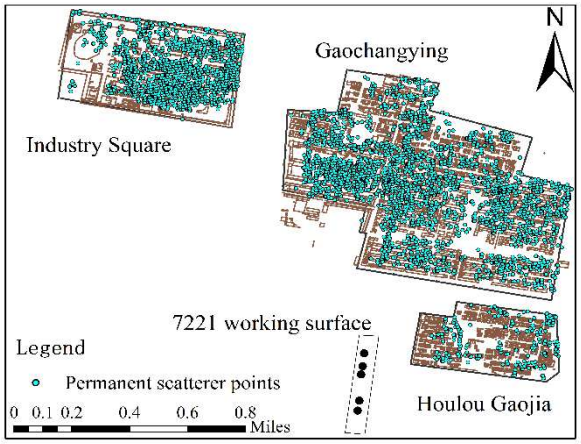

Figure 7 Spatial distribution of PS points within the village maintenance belt

Due to the large number and dense distribution of PS points within the village, it was not possible to conduct a cumulative subsidence and subsidence velocity analysis of PS points to fully utilize the data. This paper proposes a method based on the principle of permutation and combination, assuming PS points as surface deformation observation conductor points, making comprehensive observation and calculation of the geographic location and time series subsidence values of all PS points in the village, and selecting pairs of PS points with a spatial distance of 3m~30m to form the incline value calculation interval. Due to the small number of PS point pairs with calculated incline values exceeding the 3mm/m threshold during the initial time period of work face mining, the value available for analysis is low. Therefore, this paper selects 2017-10-11 - 2018-02-08, 2017-10-11 - 2018-03-04, 2017-10-11 - 2018-04-09, 2017-10-11 - 2018-05-03, 2017-10-11 - 2018-05-27, 2017-10-11 - 2018-06-20 for a total of 6 periods of incline calculations of the time-space distribution of overrun PS point pairs for the diagram. Set the diagram out period of 24 days, for the time period of intense surface deformation, the technology can still reduce the period of comprehensive observation and analysis to 12 days. The time-space distribution of the calculated incline value exceedance point pairs for PS within the village maintenance belt is shown in Figure 8.

Analysis of Figure 8 shows that the number of exceedances of the incline value of the conductor observation interval at the PS point of Houlou Gaojia Village to the composition point is very rare. The observation interval of the conductor of the composition point of the PS point pairs in Gaochangying village are concentrated in the area of exceedance in the figure near the square on the west side of the village, and the number of PS point pairs with exceeded incline values increases with the growth of the observation time interval, but the distribution range is relatively fixed. The observation interval of the conductor of the composition point of the Industrial Square PS point pairs are more scattered in the distribution of the exceeded area in the figure, and the number of PS point pairs with exceeded tilt values increases with the growth of the observation time interval, and the distribution range is spread all over the Industrial Square.

Figure 8 Spatial distribution of incline value exceedance point pairs for PS within the village maintenance belt

The PS point pairs of Houlou Gaojia Village, Gaochangying Village, and the maintenance belt of the Industrial Square are calculated by satisfying the spatial distance requirement of all PS points, and the number of conductor observation intervals, the number of overrunning point pairs, and the proportion of overrunning point pairs constituted by the obtained PS point pairs are tabulated and analyzed, and Table 2 can be obtained. Corresponding to the spatial distribution of PS points within the village maintenance belt to calculate the incline value exceedance point pairs Figure 8(a) to (f) for a total of 6 periods. The incline calculation interval composed of 854 pairs of PS points meeting the distance requirement is calculated in Houlou Gaojia Village, among which there are less than inclination calculation intervals exceeding the limit, and the proportion of the inclination calculation interval exceeding the limit in all inclination calculation intervals does not exceed 0.23%. A total of 25,933 incline calculation intervals composed of PS point pairs satisfying the distance requirement were calculated in Gaochangying village, among which less than 70 inclination calculation intervals exceeded the limit, and the proportion of the inclination calculation intervals

that exceeded the limit in all inclination calculation intervals did not exceed 0.24%. A total of 17,401 incline calculation intervals composed of PS point pairs satisfying the distance requirements were calculated for the Industrial Square, among which less than 50 incline calculation intervals exceeded the limit, and the proportion of the incline calculation intervals that exceeded the limit in all incline calculation intervals did not exceed 0.28%.

Table 2 Calculation table of incline interval overrun of Villages and Industrial Square

Incline calculation interval exceeds the number and proportion	Houlou Gaojia village incline calculation interval overruns condition	Gaochangying village incline calculation interval overruns condition	Industrial Square incline calculation interval overruns condition
2018-02-08 incline calculation of interval the number of overruns	2	12	8
2018-02-08 incline calculation interval overruns proportion	0.23%	0.046%	0.046%
2018-03-04 incline calculation of interval the number of overruns	0	21	8
2018-03-04 incline calculation interval overruns proportion	0	0.081%	0.046%
2018-04-09 incline calculation of interval the number of overruns	0	22	6
2018-04-09 incline calculation interval overruns proportion	0	0.085%	0.034%
2018-05-03 incline calculation of interval the number of overruns	0	28	6
2018-05-03 incline calculation interval overruns proportion	0	0.11%	0.034%
2018-05-27 incline calculation of interval the number of overruns	0	39	22
2018-05-27 incline calculation interval overruns proportion	0	0.15%	0.13%
2018-06-20 incline calculation of interval the number of overruns	1	62	48
2018-06-20 incline calculation interval overruns proportion	0.12%	0.24%	0.28%

The results of the incline calculation interval that meet the requirements are used as known data to calculate the curvature values within the curvature calculation interval for three important buildings in Houlou Gaojia Village, Gaochangying Village, and Industrial Square. The same dates as the incline calculation interval were chosen to calculate the maximum curvature values for buildings in these three village maintenance belts. The PS point pairs at the end-points of the curvature calculation interval exceeding $0.2(\times 10^{-3}/\mathrm{m})$ were plotted to analyze the spatial distribution in time of the PS point pairs exceeding the calculated curvature values at the surface.

The spatial distribution of the curvature calculation interval endpoints PS point pairs for the calculated curvature values exceeded within the maintenance belt of Houlou Gaojia Village is shown in Figure 9. The date selection is the same as that of the PS point pair distribution diagram of the

endpoints of the incline calculation interval of Houlou Gaojia Village. From the analysis of (a) to (f) in Figure 9, it can be seen that the number of calculated curvature values exceeding the threshold in the curvature calculation interval of Houlou Gaojia Village is small and concentrated, mainly distributed in the northeast of the village near the village maintenance belt and near the village square. In the southwest of the village, the nearest area to the 7221 working face does not have the calculated curvature value exceeding the threshold, which is less affected by the mining of the 7221 working face and has higher building stability.

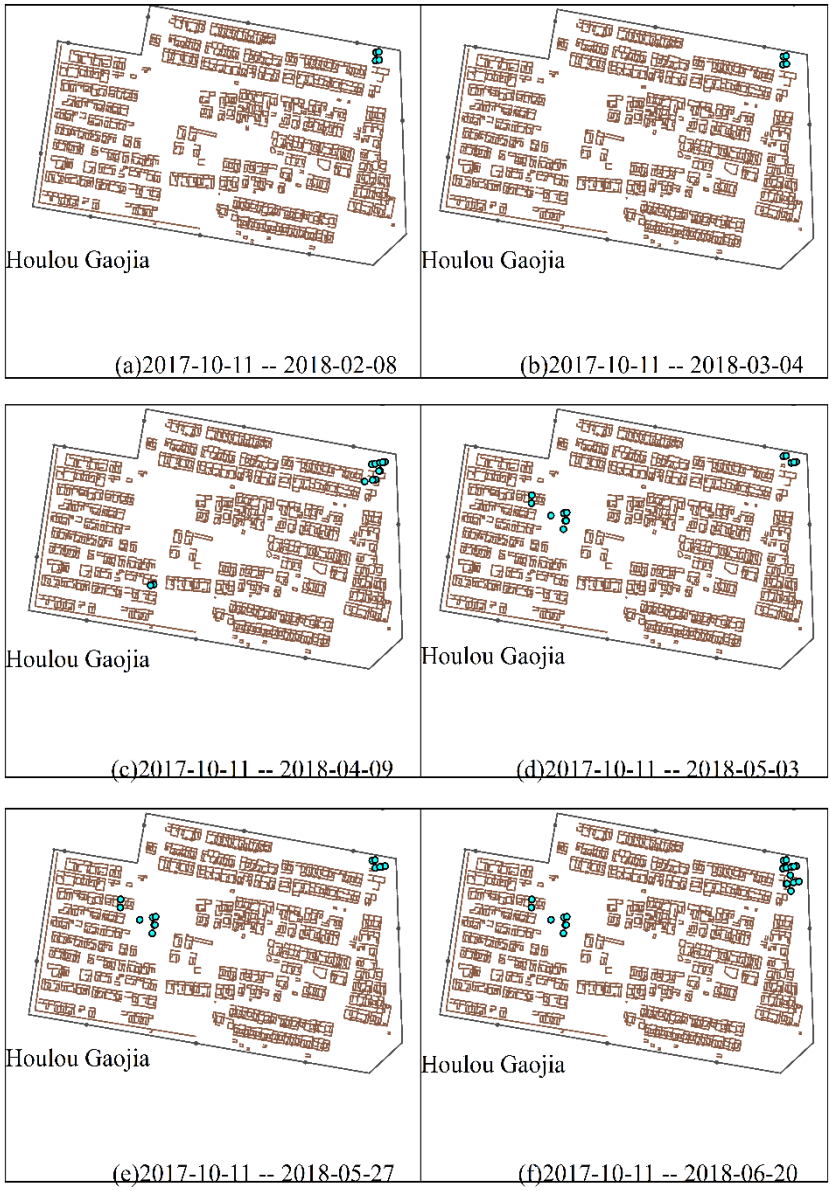

Figure 9 Spatial distribution of curvature value exceeded PS point pairs of Houlou Gaojia Village

The number of PS point pairs of curvature calculation interval endpoints in the maintenance belt of Houlou Gaojia Village is small, anto analyze the proportion of the curvature calculation interval that exceeds the limit among all curvature calculation intervals in Houlou Gaojia Village, Table 3 was made. The total number of curvature calculation intervals in Houlou Gaojia Village is 7,255, of which the number of curvature calculation intervals exceeding the limit does not exceed 30 and the proportion does not exceed 0.39%.

Table 3 Calculation table of curvature interval overrun of Houlou Gaojia Village

Curvature calculation interval statistics date	Curvature calculation interval exceeds the number of limits	Curvature calculation interval overrun proportion
2018-02-08	2	0.028%
2018-03-04	2	0.028%
2018-04-09	6	0.0845
2018-05-03	8	0.11%
2018-05-27	11	0.15%
2018-06-20	28	0.39%

The spatial distribution of the curvature calculation interval endpoints PS point pairs for the calculated curvature value exceeded within the maintenance belt of Gaochangying village is shown in Figure 10. It can be seen that the number of exceedances in the curvature calculation interval is large in Gaochangying village, but the distribution is relatively concentrated in three areas, which are the square on the west side of the village, around the buildings on the northeast side of the village and near the maintenance belt on the northwest side of the village. The buildings are easily damaged in these three areas, so monitoring and protection should be strengthened. The spatial distribution of the curvature calculation interval of the exceedance in other areas within the village is relatively scattered, and the reasons for the exceedance should be analyzed by field inspection against the spatial location distribution in the diagram.

Figure 10 Spatial distribution of curvature value exceeding PS point pairs of Gaochangying village

To specifically analyze the proportion of the number of exceeded curvature calculation intervals in the total number of curvature calculation intervals within the maintenance belt of Gaochangying village, Table 4 was obtained. The total number of curvature calculation intervals in Gaochangying Village is 752088, of which the number of curvature calculation intervals exceeding the limit does not exceed 7000 and the proportion does not exceed 0.91%. Since a curvature calculation interval needs to be expressed with the help of three PS points, the number of PS point pairs at the endpoints of the curvature calculation interval of the overrun is high and the spatial distribution is dense.

Table 4 Calculation table of curvature interval overrun of Gaochangying village

Curvature calculation interval statistics date	Curvature calculation interval exceeds the number of limits	Curvature calculation interval overrun proportion
2018-02-08	5065	0.67%

2018-03-04	2925	0.39%
2018-04-09	6870	0.91%
2018-05-03	6135	0.82%
2018-05-27	5050	0.67%
2018-06-20	6365	0.85%

The spatial distribution of the PS point pairs at the endpoints of the curvature calculation interval where the calculated curvature values are exceeded within the Industrial Square maintenance belt is shown in Figure 11. The curvature calculation interval endpoint PS point pairs of Industrial Square overruns are mainly distributed on the east side of the Industrial Square and mostly on the internal road surface of the Industrial Square, which is caused by the large number of coal trucks passing through the Industrial Square every day. The curvature calculation interval endpoint PS point pairs for the overruns in the Industrial Square buildings are also mostly close to the internal pavement of the Industrial Square. The west of the Industrial Square is a coal processing plant, there is coal, gangue open pile, so this place due to the low spatial coherence, the number of PS points is less, resulting in the curvature of the exceedance calculation interval endpoint PS point pairs are rarely distributed in the west of the Industrial Square. This place due to the accumulation pressure of coal, gangue, the surface changes drastically, instead should strengthen the monitoring and protection.

Figure 11 Spatial distribution of curvature value exceeding PS point pairs of Industrial Square

To specifically analyze the proportion of the number of curvature calculation intervals that exceed the limit in the total number of curvature calculation intervals in Industrial Square, Table 5 was made. The total number of curvature calculation intervals in industrial plazas is 417,551, of which the number of curvature calculation intervals exceeding the limit does not exceed 2,500 and the proportion does not exceed 0.59%. Since a curvature calculation interval needs to be expressed with the help of three PS points, the curvature calculation interval of the overrun involves a larger number of endpoint PS point pairs and a denser spatial distribution.

Table 5 Calculation table of curvature interval overrun of Industrial Square

Curvature calculation interval statistics date	Curvature calculation interval exceeds the number of limits	Curvature calculation interval overrun proportion
2018-02-08	492	0.12%
2018-03-04	1055	0.25%

2018-04-09	2477	0.59%
2018-05-03	948	0.23%
2018-05-27	549	0.13%
2018-06-20	736	0.18%

6 Discussion of the results

6.1 Analysis of SBAS-InSAR surface subsidence monitoring

Compared with ordinary geodetic and GPS monitoring methods, the biggest advantage of InSAR is the acquisition of plane area data. Compared with the D-InSAR, the SBAS-InSAR can select the time-space baseline threshold to remove the interferogram with poorer interference effect and effectively suppress the spatial decoherence. For the analysis of surface subsidence, SBAS-InSAR can reject the pixels with coherence lower than the threshold value and ensure the accuracy of subsidence image metadata. Meanwhile, the SBAS-InSAR also makes good improvements in the application of surface subsidence in mining areas for the problems of rapid surface subsidence and large changes in the backscattering properties of the features. In this paper, SBAS-InSAR is chosen to analyze the dynamics of the surface subsidence problem caused by the mining of the 7221 grouted working face. The results obtained by SBAS-InSAR (Figure 3) can accurately reflect the temporal and spatial extent of surface subsidence initiation and rapid subsidence in the mining area, which provides a good data basis for the analysis of surface dynamics. Then, with the help of the theory of directional derivatives, each pixel is assumed to be a "surface deformation observation line point", so that the maximum incline and curvature value of the mining area is calculated in pixel units. As shown in the figures (Figure 4 and Figure 5), the maximum incline value of the mine surface, the dynamic change of the curvature value, and the time period and spatial distribution of the surface subsidence and uplift phenomenon occurring drastically during the mining process of 7221 grouting face. To provide suggestions for the location and observation period encryption of surface movement observation wires during the mining process at the working face, and the construction of isolation zones for key protection buildings.

Due to the distance direction of the satellite, the azimuthal spatial resolution is low, which leads to the edge length of 12.75m for each pixel in the subsidence diagram calculated by SBAS-InSAR. The calculated subsidence value of each pixel is the average value of subsidence within the coverage of the pixel plane, while the actual surface deformation observation guide point measured data is the subsidence value of the measurement point. Therefore, the subsidence value obtained is smaller than the calculated value observed by the actual deployment of the surface movement observation wire, as can be obtained from the analysis in Figure 12. Then, for the corresponding incline and curvature values, the calculated results will also result in lower values than the measured ones. Evaluation of damage to buildings can result in incorrect evaluation and unreasonable protection of vulnerable buildings due to low calculated values of surface subsidence. For the regional deformation monitoring analysis with high coherence and a large number of PS points, the inversion analysis method based on the calculation interval of the PS point pair incline value and the curvature value calculation interval proposed in this paper can be selected.

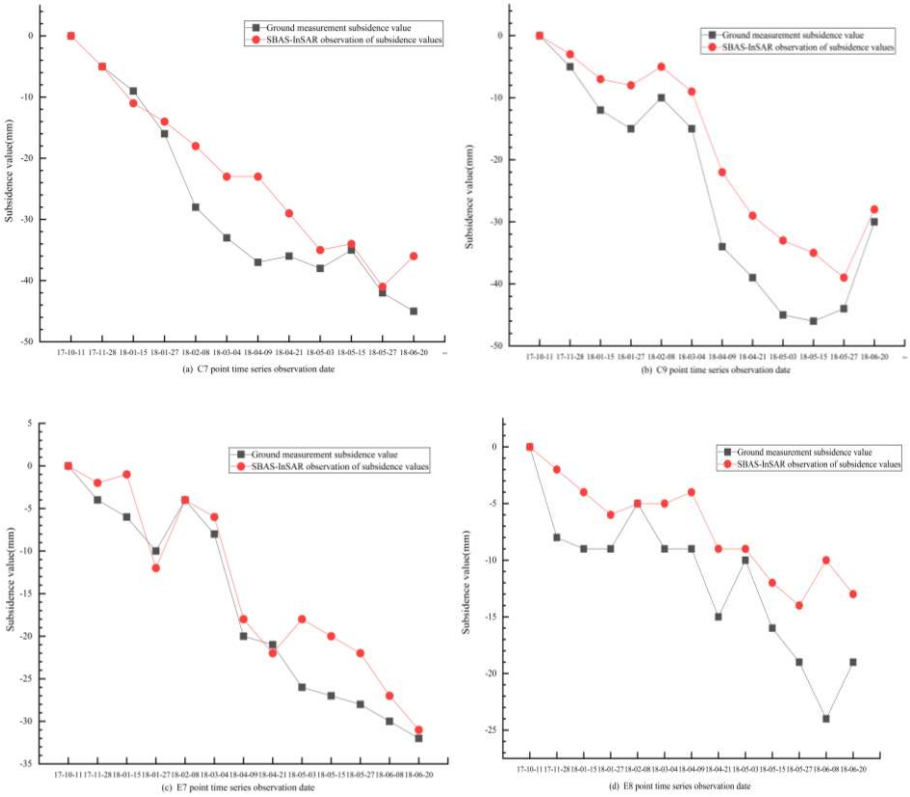

Fig. 12 Comparison of SBAS-InSAR and geodetic measurements control point subsidence values

6.2 Analysis of PS-InSAR mining surface monitoring

It is aimed at the phenomenon that the pixels in the subsidence diagram calculated by SBAS-InSAR are assumed to be surface deformation observation conductor points, and the results of calculating the surface subsidence values of buildings are small, which cannot reasonably evaluate and analyze the damage of buildings. It is proposed that the PS points in the mine area are assumed to be surface deformation observation conductor points, so that the theoretical model of incline value and curvature value calculation and analysis can be established. The following conclusions were obtained from the monitoring and analysis of the surface of the buildings within the maintenance belt of the village near the 7221 grouting work face：(1) The PS points in the maintenance belt of the mining village are assumed to be surface deformation observation conductor points, and the distance requirement of adjacent surface deformation observation conductor points is set, so that a huge number of incline calculation intervals and curvature calculation intervals can be obtained and meet the requirements. Big data damage evaluation of buildings in mining areas and spatial distribution analysis of building vulnerable areas can effectively provide suggestions for building damage evaluation and protection of key buildings. (2) The incline calculation interval and curvature calculation interval obtained by this method are not directional, and the resultant data are redundant, so how to use the data set more fully and rationally is a current problem that needs to be solved. (3) Since the principle of PS-InSAR is to select features with high coherence for subsidence analysis, the solution for applying PS-InSAR to the surface near the mine working face is to deploy artificial angle reflectors, which requires a lot of human and material resources, otherwise the number of PS points near the mine working face cannot meet the calculation requirements. Therefore, in this paper, only the PS points within the village maintenance belt are selected for analysis, and the

surface PS points near the working face cannot be analyzed.

7 Conclusion

In this paper, 21 scenes of Sentinel-1A images were selected as the data source, and the starting and ending times included the mining cycle of 7221 grout working face in a mine of Huaibei Mining Group, Anhui Province. SBAS-InSAR and PS-InSAR were used to analyze and calculate the data, focusing on deformation monitoring and building damage analysis of the ground surface within the village maintenance belt of the mining area, as well as to obtain the movement of nearby rock layers triggered by the mining of 7221 grouting work face. The specific conclusions are as follows:

From the time series subsidence diagram(Fig. 3) obtained by SBAS-InSAR calculation, it can be found that the surface subsidence affected by the Grout-filled mining technology is reduced due to the grouting activity during the working face mining process, and the active period when the surface activity is intense appears later but lasts longer. In general, the mining of 7221 grouting face has less impact on the nearest Houlou Gaojia village, while the drastic surface deformation of Gaochangying village and Industrial Square, which are farther away, is not caused by the mining of 7221 working face.

The subsidence results calculated by SBAS-InSAR are used as the data source, and the pixels are assumed to be surface deformation observation conductor points for the calculation of the maximum incline and maximum curvature value of the mine surface. It can be dynamically observed from the diagram that due to the mining of 7221 grouting face, the surface deformation extends outward from the working face area to the inside of the village maintenance belt of Houlou Gaojia Village. The calculation results of this theoretical model can also reflect the spatial distribution of active surface deformation areas in the village more accurately, and provide suggestions for monitoring and protecting the building deformation in this area.

The subsidence results of PS points calculated by PS-InSAR are used as the data source, and the PS points are hypothetically used as surface deformation observation conductor points to carry out the calculation interval of surface incline and curvature calculation interval analysis, and a large number of calculation results are obtained. For the analysis of the large data set, it was concluded that the proportion of the number of PS point pairs exceeding Class I damage within the maintenance belt of Houlou Gaojia Village, Gaochangying Village, and Industrial Square around the mine area were all less than 1% of the total calculated results. The buildings are very little affected by the mining movement of the working face during the monitoring cycle, and each incline of the village buildings, the overall value of the curvature calculation is within the threshold requirements of the I level of damage, and the few areas that exceed the threshold requirements of the I level of damage have a regular spatial distribution. Guidance can be provided for the monitoring of surface time series deformation of buildings in the maintenance belts of villages in mining areas and the key protection of buildings. The calculation results of this paper can also be used to lay conductors in the area of intense surface movement and buildings easily damaged, and to carry out encrypted observation.

Acknowledgements The authors are grateful to anonymous reviewers for their valuable suggestions.

Funding This research was supported by the National Natural Science Foundation of China [41971401]; the Fundamental Research Funds for the Central Universities [2021YJSDC17; 2021YJSDC16].

Compliance with ethical standards

Conflict of interest The authors declare that they have no conflict of interest.

Reference

Bell, F. G., T. R. Stacey, and D. D. Genske. 2000. "Mining subsidence and its effect on the environment: some differing examples." *Environmental Geology* 40 (1-2):135-52. doi: 10.1007/s002540000140.

Berardino, P., G. Fornaro, R. Lanari, and E. Sansosti. 2002. "A new algorithm for surface deformation monitoring based on small baseline differential SAR interferograms." *Ieee Transactions on Geoscience and Remote Sensing* 40 (11):2375-83. doi: 10.1109/tgrs.2002.803792.

Bhattacharya, A., and K. Mukherjee. 2017. "Review on InSAR based displacement monitoring of Indian Himalayas: issues, challenges and possible advanced alternatives." *Geocarto International* 32 (3):298-321. doi: 10.1080/10106049.2016.1140820.

Castaneda, C., F. Gutierrez, M. Manunta, and J. P. Galve. 2009. "DInSAR measurements of ground deformation by sinkholes, mining subsidence, and landslides, Ebro River, Spain." *Earth Surface Processes and Landforms* 34 (11):1562-74. doi: 10.1002/esp.1848.

Chen, J. L., Y. Zhou, G. Chen, and M. Hao. 2021. "Decades of Ground Deformation in the Weihe Graben, Shaanxi Province, China, in Response to Various Land Processes, Observed by Radar Interferometry and Levelling." *Remote Sensing* 13 (12):16. doi: 10.3390/rs13122374.

Comerci, V., E. Vittori, C. Cipolloni, P. Di Manna, L. Guerrieri, S. Nisio, C. Succhiarelli, M. Ciuffreda, and E. Bertoletti. 2015. "Geohazards Monitoring in Roma from InSAR and In Situ Data: Outcomes of the PanGeo Project." *Pure and Applied Geophysics* 172 (11):2997-3028. doi: 10.1007/s00024-015-1066-1.

Diao, X. P., Z. H. Bai, K. Wu, D. W. Zhou, and Z. L. Li. 2018. "Assessment of mining-induced damage to structures using InSAR time series analysis: a case study of Jiulong Mine, China." *Environmental Earth Sciences* 77 (5):14. doi: 10.1007/s12665-018-7353-2.

Ding, P. P., C. Jia, S. T. Di, J. Wu, and R. C. Wei. 2021. "Analysis and Evaluation of Land Subsidence along Linear Engineering Based on InSAR Data." *Ksce Journal of Civil Engineering* 25 (9):3477-91. doi: 10.1007/s12205-021-0201-z.

Du, Q. S., G. Y. Li, Y. Zhou, M. T. Chai, D. Chen, S. S. Qi, and G. Wu. 2021. "Deformation Monitoring in an Alpine Mining Area in the Tianshan Mountains Based on SBAS-InSAR Technology." *Advances in Materials Science and Engineering* 2021:15. doi: 10.1155/2021/9988017.

Fan, H. D., L. Lu, and Y. H. Yao. 2018. "Method Combining Probability Integration Model and a Small Baseline Subset for Time Series Monitoring of Mining Subsidence." *Remote Sensing* 10 (9):18. doi: 10.3390/rs10091444.

Ferretti, A., C. Prati, and F. Rocca. 2000. "Nonlinear subsidence rate estimation using permanent scatterers in differential SAR interferometry." *Ieee*

Transactions on Geoscience and Remote Sensing 38 (5):2202-12. doi: 10.1109/36.868878.

Gao, J. X., H. Hu, F. Liu, Z. K. Li, and Y. F. Yao. 2014. "Signal extraction for GPS deformation monitoring in mining survey." *Transactions of Nonferrous Metals Society of China* 24 (12):3949-54. doi: 10.1016/s1003-6326(14)63555-x.

Hooper, A., P. Segall, and H. Zebker. 2007. "Persistent scatterer interferometric synthetic aperture radar for crustal deformation analysis, with application to Volcan Alcedo, Galapagos." *Journal of Geophysical Research-Solid Earth* 112 (B7):21. doi: 10.1029/2006jb004763.

Hooper, A., H. Zebker, P. Segall, and B. Kampes. 2004. "A new method for measuring deformation on volcanoes and other natural terrains using InSAR persistent scatterers." *Geophysical Research Letters* 31 (23):5. doi: 10.1029/2004gl021737.

Kumar, S., D. Kumar, S. K. Chaudhary, N. Singh, and K. K. Malik. 2020. "Land subsidence mapping and monitoring using modified persistent scatterer interferometric synthetic aperture radar in Jharia Coalfield, India." *Journal of Earth System Science* 129 (1):10. doi: 10.1007/s12040-020-01413-0.

Li, J. C., F. Gao, and J. G. Lu. 2019. "An application of InSAR time-series analysis for the assessment of mining-induced structural damage in Panji Mine, China." *Natural Hazards* 97 (1):243-58. doi: 10.1007/s11069-019-03639-8.

Li, M. H., L. Zhang, M. S. Liao, and X. G. Shi. 2016. "Detection of coal-mining-induced subsidence and mapping of the resulting deformation using time series of ALOS-PALSAR data." *Remote Sensing Letters* 7 (9):855-64. doi: 10.1080/2150704x.2016.1193794.

Li, X., G. W. Huang, Q. Zhang, and Q. Z. Zhao. 2018. "A new GPS/BDS tropospheric delay resolution approach for monitoring deformation in super high-rise buildings." *Gps Solutions* 22 (3):12. doi: 10.1007/s10291-018-0752-8.

Li, Z., J. M. Zhou, B. S. Tian, and Ieee. 2009. THE GLACIER MOVEMENT ESTIMATION AND ANALYSIS WITH INSAR IN THE QINGHAI-TIBETAN PLATEAU. Paper presented at the IEEE International Geoscience and Remote Sensing Symposium, Cape Town, SOUTH AFRICA, Jul 12-17.

Maghsoudi, Y., F. van der Meer, C. Hecker, D. Perissin, and A. Saepuloh. 2018. "Using PS-InSAR to detect surface deformation in geothermal areas of West Java in Indonesia." *International Journal of Applied Earth Observation and Geoinformation* 64:386-96. doi: 10.1016/j.jag.2017.04.001.

Mastro, P., C. Serio, G. Masiello, and A. Pepe. 2020. "The Multiple Aperture SAR Interferometry (MAI) Technique for the Detection of Large Ground Displacement Dynamics: An Overview." *Remote Sensing* 12 (7):48. doi: 10.3390/rs12071189.

Moreira, A., P. Prats-Iraola, M. Younis, G. Krieger, I. Hajnsek, and K. P. Papathanassiou. 2013. "A Tutorial on Synthetic Aperture Radar." *Ieee Geoscience and Remote Sensing Magazine* 1 (1):6-43. doi: 10.1109/mgrs.2013.2248301.

Olivier, G., F. Brenguier, R. Carey, P. Okubo, and C. Donaldson. 2019. "Decrease in Seismic Velocity Observed Prior to the 2018 Eruption of Klauea Volcano With

Ambient Seismic Noise Interferometry." *Geophysical Research Letters* 46 (7):3734-44. doi: 10.1029/2018gl081609.

Samsonov, S., N. d'Oreye, and B. Smets. 2013. "Ground deformation associated with post-mining activity at the French-German border revealed by novel InSAR time series method." *International Journal of Applied Earth Observation and Geoinformation* 23:142-54. doi: 10.1016/j.jag.2012.12.008.

Sedlak, V., and Sgem. 2015. THE POSSIBILITY OF SPECIFIC SOLUTIONS OF DEFORMATIONS IN THE UNDERMINED AREAS. Paper presented at the 15th International Multidisciplinary Scientific Geoconference (SGEM), Albena, BULGARIA, Jun 18-24.

Shi, Y., Q. W. Li, X. Meng, T. K. Zhang, and J. J. Shi. 2020. "On Time-Series InSAR by SA-SVR Algorithm: Prediction and Analysis of Mining Subsidence." *Journal of Sensors* 2020:17. doi: 10.1155/2020/8860225.

Sui, L. C., F. Ma, and N. Chen. 2020. "Mining Subsidence Prediction by Combining Support Vector Machine Regression and Interferometric Synthetic Aperture Radar Data." *Isprs International Journal of Geo-Information* 9 (6):17. doi: 10.3390/ijgi9060390.

Tang, W., W. Zhan, B. W. Jin, M. Motagh, and Y. B. Xu. 2021. "Spatial Variability of Relative Sea-Level Rise in Tianjin, China: Insight From InSAR, GPS, and Tide-Gauge Observations." *Ieee Journal of Selected Topics in Applied Earth Observations and Remote Sensing* 14:2621-33. doi: 10.1109/jstars.2021.3054395.

Wang, Z. Y., J. X. Zhang, G. M. Huang, and Y. H. Zhang. 2009. Monitoring land subsidence in Suzhou city using D-InSAR technique. Paper presented at the 2nd International Congress on Image and Signal Processing, Tianjin, PEOPLES R CHINA, Oct 17-19.

Wesolowski, M. 2016. "THE POSSIBILITIES OF USING ANISOTROPIC MODELS OF ROCK MASS TO DESCRIBE DEFORMATIONS OF THE MINING AREA SURFACE." *Archives of Mining Sciences* 61 (1):125-36. doi: 10.1515/amsc-2016-0010.

Xing, X. M., J. J. Zhu, Y. Z. Wang, and Y. F. Yang. 2013. "Time series ground subsidence inversion in mining area based on CRInSAR and PSInSAR integration." *Journal of Central South University* 20 (9):2498-509. doi: 10.1007/s11771-013-1762-x.

Yang, Z. F., Z. W. Li, J. J. Zhu, Y. D. Wang, and L. X. Wu. 2020. "Use of SAR/InSAR in Mining Deformation Monitoring, Parameter Inversion, and Forward Predictions: A Review." *Ieee Geoscience and Remote Sensing Magazine* 8 (1):71-90. doi: 10.1109/mgrs.2019.2954824.

Zhang, W. J., W. H. Wang, and L. W. Chen. 2012. Constructing DEM Based on InSAR and the Relationship between InSAR DEM's Precision and Terrain Factors. Paper presented at the International Conference on Future Energy, Environment, and Materials (FEEM), Hong Kong, PEOPLES R CHINA, Apr 12-13.

Zhou, J. M., Z. Li, X. W. Li, S. Y. Liu, Q. Chen, C. Xie, and B. S. Tian. 2011. "Movement estimate of the Dongkemadi Glacier on the Qinghai-Tibetan Plateau using L-band and C-band spaceborne SAR data." *International Journal of Remote Sensing* 32 (22):6911-28. doi: 10.1080/01431161.2010.517225.

1
2